2D CO CRS IMAGING FOR MULTICOMPONENT DATA RECORDED BY THE VSP GEOMETRY

M. von Steht

email: *Markus.vonSteht@gpi.uni-karlsruhe.de*

keywords: *CRS stack, VSP, common offset, kinematic wavefield attributes, multicomponent*

ABSTRACT

In this paper a new sophisticated design for a processing sequence to analyze walkaway prestack data recorded with the vertical seismic profile (VSP) acquisition geometry will be introduced. The approach is based on the concepts of the common-reflection-surface (CRS) stack theory, in particular on the extension to common-offset (CO) imaging firstly introduced by Zhang et al. (2001). CRS-stack-based imaging bears the significant advantages of an increased signal-to-noise ratio, a high degree of automation throughout the processing and convenient quality control by the user.
This method results in high-quality stacked sections in which the output traces follow a certain mutual relationship being further explained in the course of this paper. The processing by means of CRS technology also yields traveltime parameters related to so-called kinematic wavefield attributes. These CRS attributes can serve as an input to imaging steps beyond stacking as, e.g., building of velocity models and time/depth migration. Recent efforts by Boelsen (2005) with the aim of extracting PP- and PS-conversions immanent in multicomponent data using CRS attributes have been very promising. By using the latter approach a coupling of a reflection event's kinematic traveltime response and the polarization of a geophone's components is achieved. My presentation attempts to cover all of the above-mentioned issues by an equal amount but has to be seen as stripped by many details for the limited extent of this report.

INTRODUCTION

The common-reflection-surface (CRS) stack was firstly presented in real-data application by Müller (1998) and represents the concept of a purely *data-driven* imaging method. The intention behind this type of design is to demand as little user-interaction as possible once the imaging process is started in order to speed-up processing time and to reduce man-made errors. This accounts for the independence of a user-supplied macrovelocity model as one fundamental aspect of the underlying theory.
The development of the CRS method also aims at the enhancement of the rather simple and straightforward conventional NMO/DMO stack by including additional properties of the underground as they can be described by, e. g., paraxial ray theory.

Common-offset (CO) stacking can be thought of to be the generalization of ZO stacking and it is performed analogously. A CO stacking operator approximates the actual reflection events in the vicinity of a given event in a CO gather corresponding to a measurement configuration with a fixed offset, i. e., a fixed distance between the sources and receivers.
This distance can either be horizontal, vertical or a combination of both as in the presented case for a VSP geometry. One might—prematurely as will be shown—object that a *bilinear relation* of two different coordinate axes should never be called an "offset" but just let us assume for now that I have justified that claim already.

One motivation to perform stacking towards a common offset is to look into regions of the subsurface poorly illuminated by normal rays. There are many situations when only seismic data at rather high source-

receiver offsets will contain substantial reflection response of the underground, e. g., in case of sub-salt imaging.
Another potential of tending towards a simulated two-way experiment is the opportunity to investigate *converted waves* in the case that multicomponent data was acquired. Separating PP- from PS events not only doubles the amount of information accumulated but also provides access to a whole range of additional parameters.
This kind of separation is not possible with ZO-based imaging methods as they assume a central ray to be a normal ray, loosing the opportunity to be converted at all, naturally.

To combine the opportunities which CO imaging creates with the methodology of the CRS stack—representing stability, high resolution, and adaptability—was a progressive step to also describe acquisition geometries like OBS, OBC or VSP. I have to point out that the presented extension is yet restricted to be applicable in 2D only.

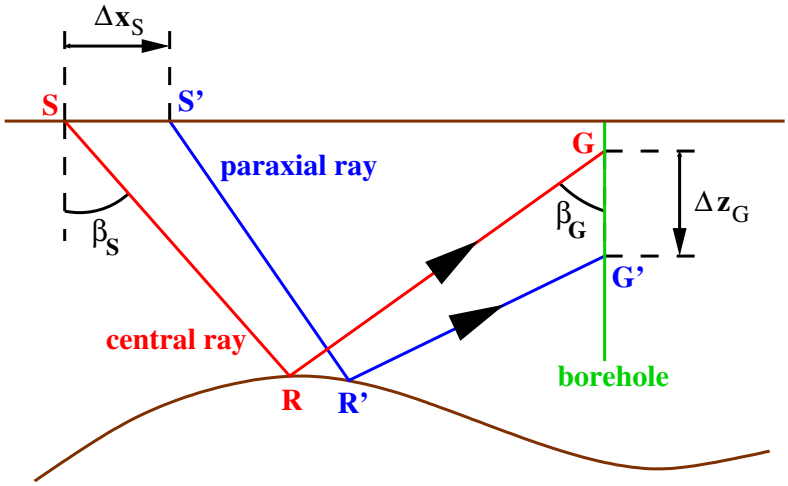

Figure 1: Visually interpretable variables of traveltime formula (2) in the context of paraxial ray theory. The acquisition geometry has been restricted for reasons of clarity only. (Image courtesy of Boelsen (2005))

CRS OPERATOR FOR VSP

The theoretical foundations for my investigations of VSP-related imaging by the CRS method are mainly derived from the ideas introduced by Zhang et al. (2001). By their effort, the so-called *common-offset CRS stack* was established as an alternative to the traditional zero-offset imaging tools for surface seismics. The term common-offset (CO) stack resembles a reorientation of the target domain for the stacking operation from monostatic to bistatic.

If I apply this statement to theory, namely to the paraxial ray theory, I also have to mention that the central rays which are generally approximated will no longer remain normal rays. The associated virtual source and receiver positions S and G from which the paraxial traveltimes immanent to the prestack data are calculated do not coincide any more.

The paraxial CO CRS traveltime operator for arbitrary topography in 2D which is the most general form possible was firstly derived in Boelsen (2005). I repeat it here not only for the sake of completeness:

$$
\begin{aligned}
\tau^2(\Delta x_S,&\Delta z_S, \Delta x_G, \Delta z_G) = \\
&\left(\tau_0 + \frac{\sin\beta_S}{v_S}\,\Delta x_S - \frac{\cos\beta_S}{v_S}\,\Delta z_S + \frac{\sin\beta_G}{v_G}\,\Delta x_G - \frac{\cos\beta_G}{v_G}\,\Delta z_G \right)^2 \\
&- 2\,\tau_0\,B^{-1}\,(\Delta x_S - \Delta z_S\,\tan\beta_S)\;(\Delta x_G - \Delta z_G\,\tan\beta_G) \\
&+ \tau_0\,AB^{-1}\,(\Delta x_S - \Delta z_S\tan\beta_S)^2 \\
&+ \tau_0\,DB^{-1}\,(\Delta x_G - \Delta z_G\tan\beta_G)^2
\end{aligned}
\tag{1}
$$

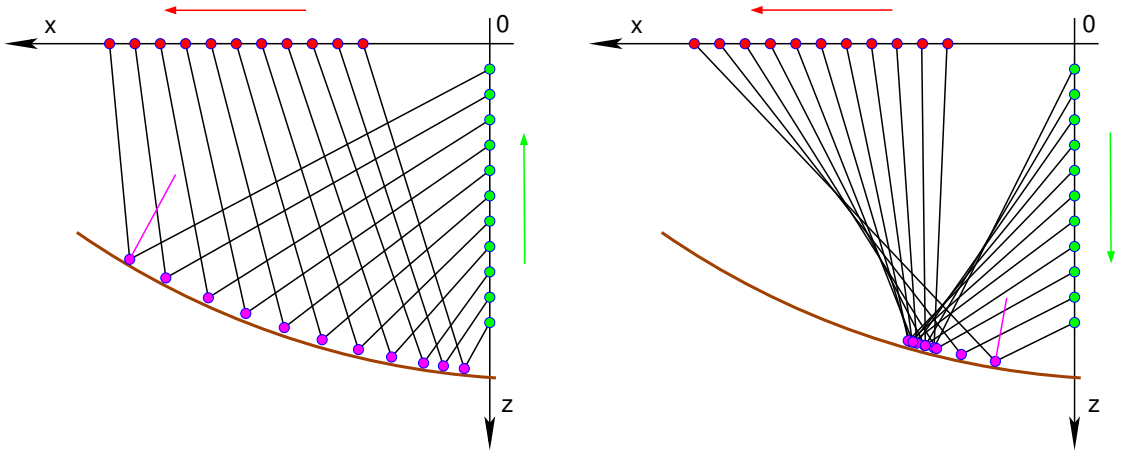

(a) Common offset-alike relation used for the presented method. It's raypaths almost evenly cover a given interface.

(b) The zero offset-alike relation covers a very limited vicinity of a point on an interface — but under different angles of incidence.

Figure 2: Possible relationships of sources and receivers.

The parameters AB^{-1}, DB^{-1}, and B^{-1} are composed by elements of the *surface-to-surface* propagator matrix (see, e.g., Červený, 2001). $\Delta x_{S/G}$ and $\Delta z_{S/G}$ indicate the horizontal and vertical displacements off the central ray. $v_{S/G}$ are the valid near-surface velocities in the paraxial vicinity of the central ray and $\beta_{S/G}$ are the emergence angles at either of its ends.

For explanatory purposes I now will simplify expression (1) to a restricted VSP geometry with a borehole pointing straight into depth. Doing so the line of shots and the line of receivers will be mutually perpendicular and it is possible to discard two degrees of freedom: $\Delta z_S \equiv 0$ and $\Delta x_G \equiv 0$:

$$\begin{aligned}\tau^2(\Delta x_S,\Delta z_G) = & \\ & \left(\tau_0 + \frac{\sin\beta_S}{v_S}\,\Delta x_S - \frac{\cos\beta_G}{v_G}\,\Delta z_G\right)^2 \\ & - 2\,\tau_0\,B^{-1}\Delta x_S\,\Delta z_G\,\tan\beta_G \\ & + \tau_0\,AB^{-1}{\Delta x_S}^2 \\ & + \tau_0\,DB^{-1}\left(\Delta z_G\tan\beta_G\right)^2\end{aligned} \tag{2}$$

By applying these restrictions on the general operator it was possible for me to run some preliminary tests on synthetic data — reducing computational time — for the purpose of conducting a feasibility study. This study proved to be promising enough (von Steht, 2006) to further pursue the issue of adapting CRS imaging to the VSP domain. The explanations given in the remaining sections will be assuming this type restricted geometry for simplicity.

I want to point out that the number of stacking parameters visible in general expression (1) does not reduce from being five even in case of a restricted or simplified geometry as displayed in Figure 1. This also means that I can use the general operator to describe very complex acquisition geometries including deviated boreholes and complex top-surface topography with no further difficulties imposed.

The fast but yet accurate determination of the emergence angles $\beta_{S/G}$ and the matrix elements AB^{-1}, DB^{-1}, and B^{-1}, the latter three being related to *wavefront curvatures* is a five dimensional optimization problem and the main objective in CRS-stack-based imaging.

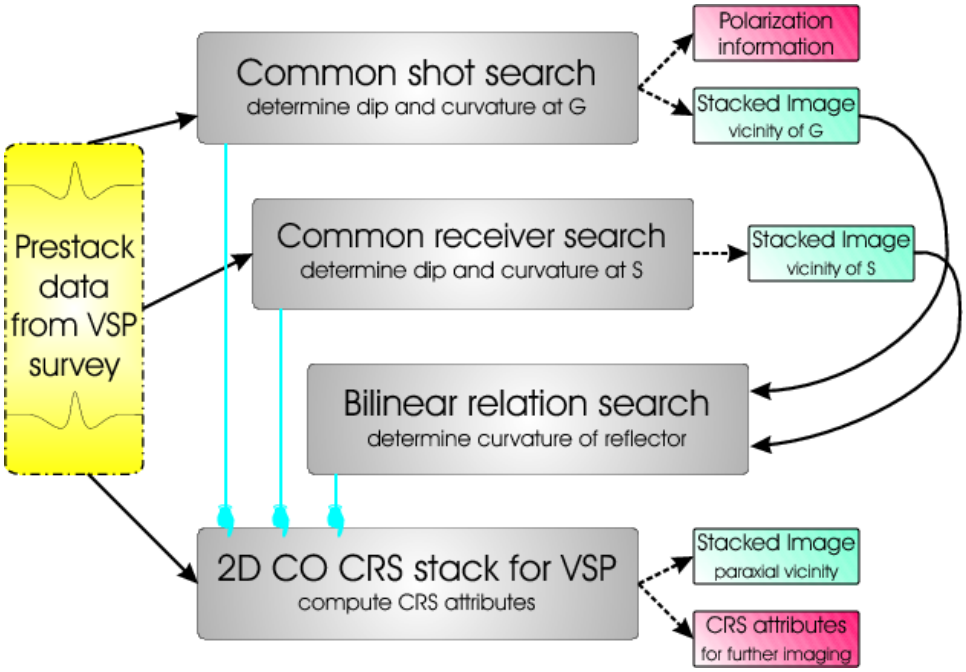

Figure 3: Sketch of necessary steps towards a CRS-stacked set of traces following the ray diagram in Figure 2(a). The processing sequence runs from top to bottom.

BILINEAR RELATIONSHIP BETWEEN SOURCE AND RECEIVER LOCATIONS

In Figures 2(a) and 2(b) two different types of bilinear relations for central rays can be observed. The rays illuminate a target reflector in very different ways depending on whether source and receiver positions both move away from the wellhead as on Figure 2(b) or whether there is an opposing movement as shown on Figure 2(a). The shape of the chosen reflection interface does not change this behavior too significantly even if I consider it to be concave or convex. For the investigation of the CO CRS method in case of a restricted VSP geometry the simulated central rays follow the relation

$$x_0 + i\,dx + z_0 + i\,dz = h_{\mathrm{VSP}} = \mathrm{const} \tag{3}$$

with increments dx and dz having opposite signs and i being the number of rays. The quasi-offset h_{VSP} can regarded to be the classical *finite offset* of surface seismics in case the borehole axis is rotated by 90 degrees.

DETERMINATION OF STACKING PARAMETERS AND WORKFLOW

If I begin by neglecting the multicomponent approach I am left with the problem of determining five stacking parameters which will provide expression (1) or its subset (2) with all the necessary terms for a proper moveout correction. This task is accomplished by coherence analysis as it is common practice in data-driven approaches — semblance is used in my implementation as a default.

In detail the analysis is carried out by three linearized parameter searches in order to stabilize and accelerate the optimization. The workflow displayed in Figure 3 describes the most significant steps and their relationships. Two subsets containing the prestack data in the common shot and common receiver domain, which are not symmetrical for the VSP case, are investigated each for an operator dip and curvature, respectively.

I want to emphasize that the positions of analyzed gathers in the recorded data and their associated expansion points related to simulated rays have to be in accordance with expression (3). In this way the obtained stacking results for CS- and CR-subsets will be kinematically equivalent so that both sets of traces can be used subsequently for a third parameter search. This part of the workflow solely will determine the

curvature across the reflection events since its dip is a composite of previously computed properties.

Once the curvature related to B^{-1} is known all five stacking parameters appearing in traveltime operator (2) are available. Finally I can stack VSP prestack traces along *CRS supergathers* resulting in a set of traces with a superior S/N ratio.

In case of a multicomponent approach I will have apply a *CRS wavefield separation* right after the first search-step in the CS domain. The calibration of geophone polarization and the CRS attributes derived from the stacking parameters is established by choosing either P-wave or S-wave velocities which have to be physically reasonable for all geophone expansion points.

Including the wavefield separation into the approach not only doubles the computational time since I have to determine twice as many stacking parameters to handle both wavetypes. It is also necessary to reorient the polarization direction of the prestack traces throughout the coherence analysis in the CS gathers *on the fly*. Only in this way the guided amplification of P-waves on the radial and S-waves on the transversal component can be achieved in a satisfying manner.

SYNTHETIC DATA EXAMPLE

I now want to introduce a synthetic data example which was provided by PAULSSON GEOPHYSICAL SERVICES INC. and served as my initial test data to run experiments on with the new approach. Figure 5(a) shows a 3D plot of the two walkover lines leaving the vertical borehole (depth up to $\approx$ 0.8 km) straight in north-south and east-west direction. There are some gaps in the shot-spacing which indicates the close relationship to an actual real data set which is under my present investigation. The acquisition surface can be described as almost planar and non-dipping, which is the total opposite to the two reflectors in depths of approximately 0.5 km and 1.0 km. For the following I want to focus on the walkover line running in north-south direction with an approximate length of 2.0 km.

The underlying inhomogeneous 3D velocity model for primary waves is depicted in Figure 5(b). Shear-wave velocities were derived from the latter by the $\sqrt{3}$-relationship as the commonly used default provided by the modeling tool, i.e.,NORSAR. There is a steep velocity gradient present in the first 300 m, which is clipped out of the displayed range but causes turning waves.

The depth-velocity curves for P- and S-waves shown in Figure 5(c) were not directly derived from the velocity model. I used a synthetic *checkshot* close to the wellhead and picked the first arrivals of the downgoing P-wave to serve as an input to a 1D inversion algorithm and smoothed down the resulting curve. The S-waves' velocities again are related by $\sqrt{3}$ to the ones of P-waves but looking at checkshots carried out with S-wave sources will result in similar functions for this example.

A glance at Figures 4(a) and 4(b) reveals how VSP common shot sections — after considerable amount of preprocessing for real data — will typically look like on two components. The displayed gathers were recorded for a source approximately 500 m north off the wellhead. Downgoing energy will be focused on the first arrivals of the P-wave either by using deconvolution operators or surgical fk-filtering. In this way the downgoing S-wave should be eliminated, respectively. The modeled raycodes for upcoming energy on both interfaces were PP, PS, and SS providing us with six events for the subsequent CRS processing.

Since space is limited for this presentation I cannot go too much into details about the actual application of the processing flow as it was introduced in the previous section. The CRS stack for the VSP geometry — like his zero offset "siblings" — provides a multitude of useful by-products and intermediate results, which can be carefully scrutinized to refine future processing steps. As an example for CRS attributes for reflected P- and S-waves I included the geophone emergence angles of 50 central rays of the northern walkaway line. I have to emphasize that β_G^{P} and β_G^{S} as shown in Figures 6(a) and 6(b) are connected to the ray diagram shown in Figure 2(a). This relationship applies to all further output created by the method as well. The displayed angles show a very broad range especially for the top reflector and generally are of high resolution which is a benefit for the role they play during the subsequently carried out wavefield separation.

The stacking result for the complete walkover line with an approximate fold of 300 traces in the paraxial vicinity for PP-events can be observed in Figure 7(a). Please note that PS- and SS-events are not discriminated due to wavefield separation techniques but merely because of the reduced range of moveout curves the traveltime operator can approximate once it is calibrated to a physical velocity v_G^{P}. The reason why the first reflector is not visible on the central traces is because their expansion points in depth are located

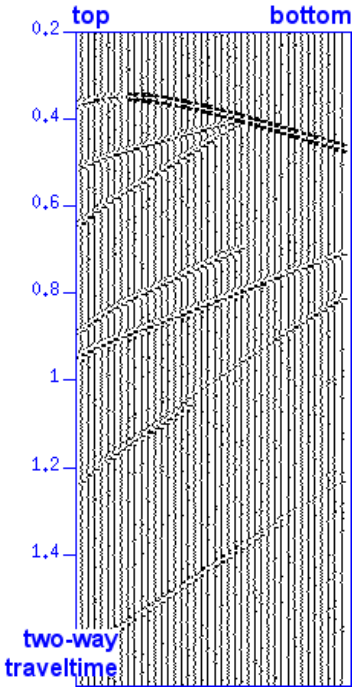

(a) V-component

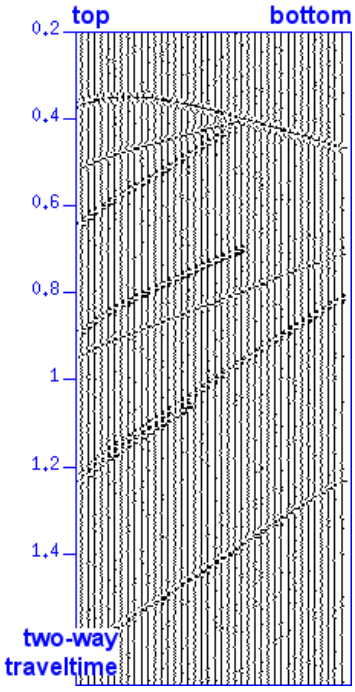

(b) H-component

Figure 4: Example common shot gather taken from the synthetic data set. Its position is approximately 500 m off the wellhead towards the north.

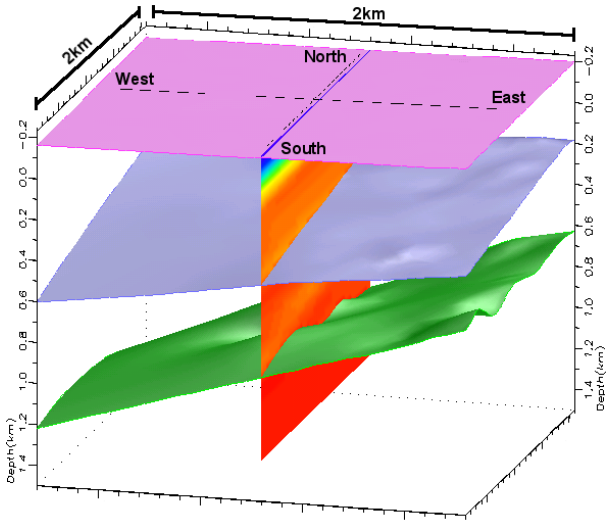

(a) View of 3D model

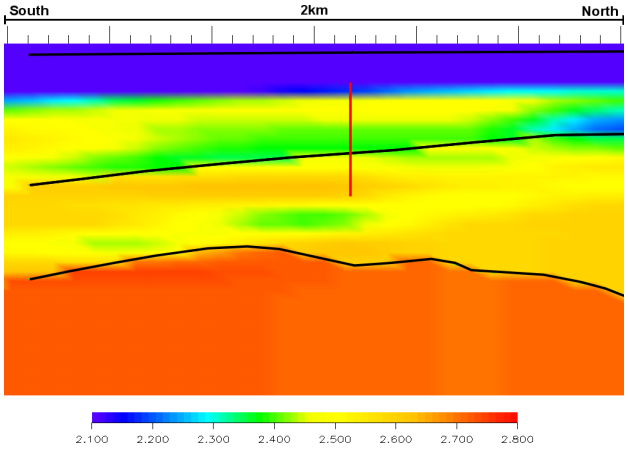

(b) P-wave velocity model

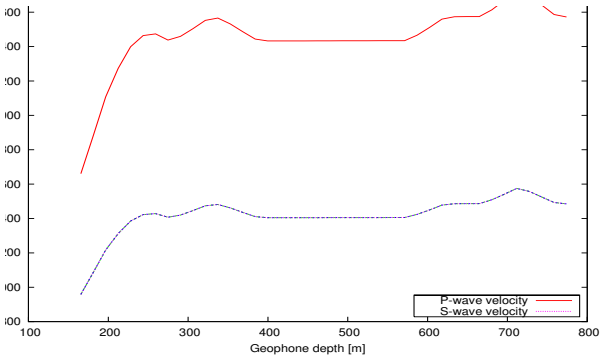

(c) Velocity-depth functions which were used to calibrate traveltime operator (2) to polarization of multicomponent geophones.

Figure 5: Description of the model used to generate the synthetic data as displayed in Figures 4(a) and 4(b).

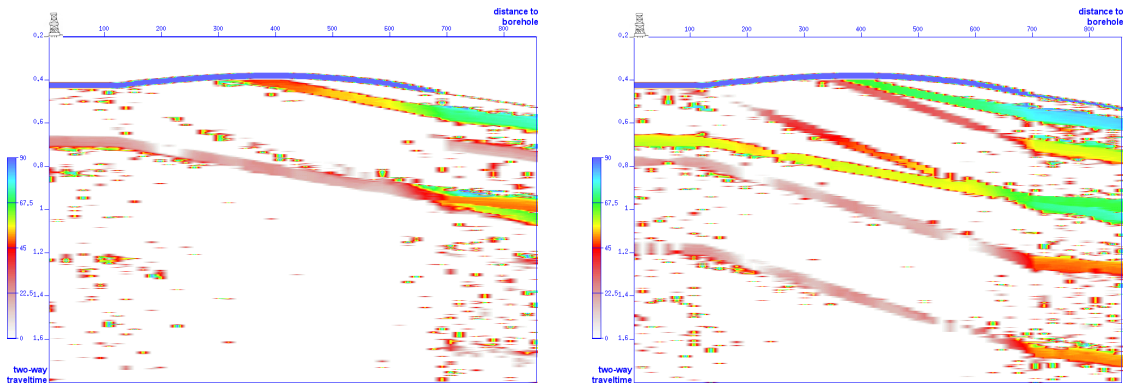

(a) Emergence angle β_G^P **(b)** Emergence angle β_G^P

Figure 6: Example of CRS attributes obtained in the course of the workflow.

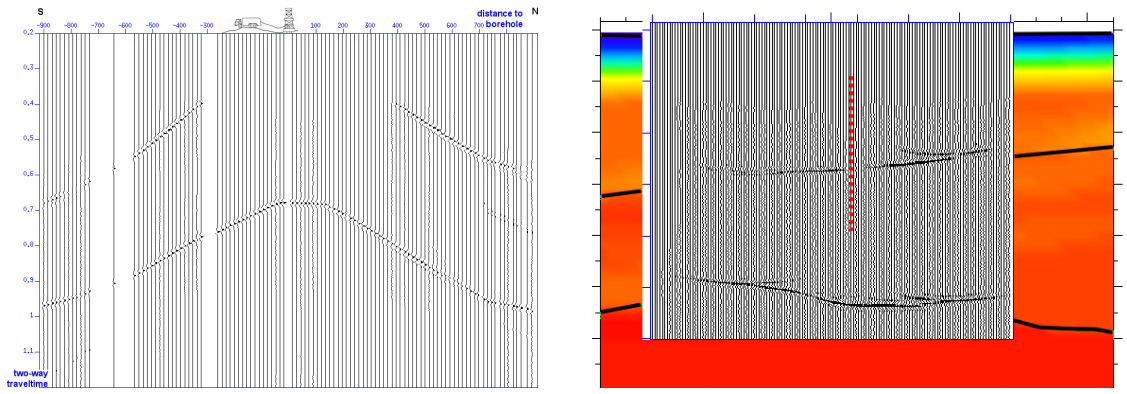

(a) VSP synthetic data - Poststack migration - input **(b)** VSP synthetic data - Poststack migration - output

Figure 7: CRS-stacked traces from northern and southern walkaway-line serving as an input for Kirchhoff PostSDM following the bilinear relation of Figure 2(a).

beneath that interface.

QUALITY ESTIMATION BY KIRCHHOFF DEPTH-MIGRATION

Since the main output created by the CO CRS processing for VSP is a set of stacked traces in the *quasi-common offset* domain any interpreter will have a hard time to visualize the subsurface at this stage. So I applied a Kirchhoff poststack depth migration to the CRS stacked traces shown in Figure 7(a) with the velocity model taken from Figure 5(b) to check for the consistency of the approach. A preliminary result which still requires considerable amount of tapering at the edges (see Figure 7(b)) confirms the accuracy of the method up to the first interface. The second interface has a different shape and it is migrated too shallow when being compared to the underlying model.

In order to have more clues to investigate the mismatch of the second interface I applied a Kirchhoff prestack depth migration with an migration aperture corresponding to all traces which had been used in the CRS stacking aperture. A magnified section of both migration results is displayed in Figures 8(a) and 8(b) and lets me draw several conclusions. The postSDM illuminates a much larger segment of both interfaces in a constantly high resolution even if I consider the avoidable migration artifacts. The preSDM has not

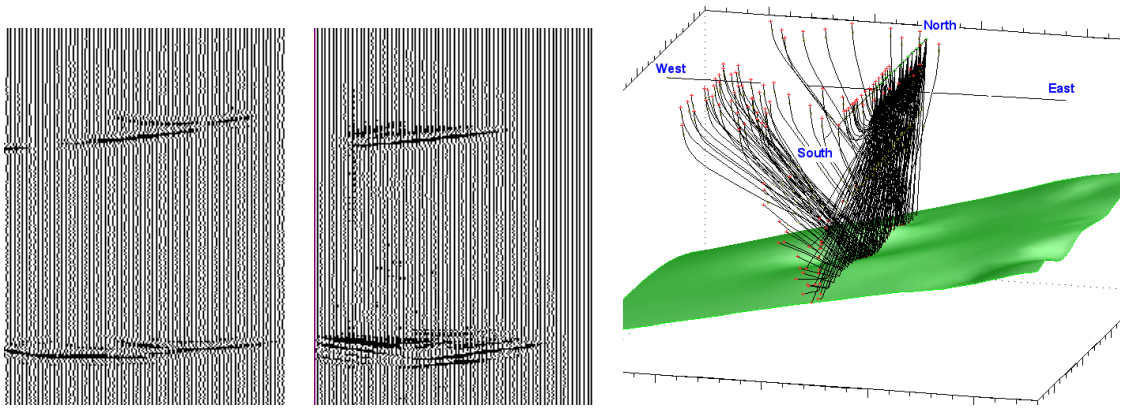

(a) PostSDM for 50 CRS-stacked traces

(b) PreSDM for $\approx$2000 traces

(c) Raytracing in 3D model reveals out-of-plane reflections.

Figure 8: Comparison between post- and prestack depth migration for VSP in a magnified view. Figure 8(c) explains the mismatch between both methods but also the displacement of the second interface as observed in Figure 7(b).

only the same mismatch in depth and shape for the second interface but furthermore is unfocused there. The benefit of imaging a *reflection surface* instead of a *reflection point* which is the dominant feature of CRS-based methods is very obvious in this example.

The issue of mismatches in depth and shape was resolved by performing several raytracing experiments in the 3D velocity model in order to backtrack the raypaths of the modeled reflection events. As it is obvious in Figure 8(c) the assumption that all wave propagation takes place in a 2D plane is certainly not valid for this model.

AN APPLICATION: CRS-BASED WAVEFIELD SEPARATION

The idea behind the separation of PP- and PS-wavefields in the CRS approach for VSP geometries is realizable with little effort. As displayed in Figure 9(a) seismic P-waves being created at point S reach an interface in the subsurface to produce a reflection event. Each reflection event mainly consists of P-wave energy but some energy will also be converted into S-waves bearing very useful additional information on the investigated underground. The points of reflection R^{P} and conversion R^{S} generally do not coincide.

Therefore, a two-component geophone placed at G will not only record PP- and PS-events originating from different directions related to the emergence angles β_G^{P} and β_G^{S}. An observed event will also be distributed on the vertical (mainly P-waves) and horizontal (usually S-waves) component of G in a thoroughly superpositioned sense according to its related emergence angle.

The proposed processing scheme includes the determination of the emergence angles β_G^{P} and β_G^{S} for a virtual geophone placed on the receiver side of a central ray. A calibration to either P- or S-wave velocity-depth functions has to be performed prior to this analysis in order to assign a true, physical meaning to both sets of CRS attributes. The attributes shown in Figures 6(a) and 6(b) have been computed in that way.

The rotation of the horizontal and vertical components of prestack data, assuming it to be linked to a *paraxial geophone* by such a determined angle yields a P-event on the radial component for a given β_G^{P}. Providing β_G^{S} will result in an S-event on the transversal component of the prestack data, respectively. Both situations are depicted in Figures 9(b) and 9(c).

Nevertheless a simple rotation by $\beta_G^{\mathrm{P/S}}$ will only work in the close vicinity of the investigated central ray, but it will not suffice to rotate the whole prestack data, accordingly.

For a complete reorientation and separation of the PP- and PS-wavefield of the prestack data I utilize the already introduced angles $\beta_G^{\mathrm{P/S}}$ and additionally the wavefield curvatures $K_{G_{\mathrm{CS}}}^{\mathrm{P/S}}$ (a composite of DB^{-1} and

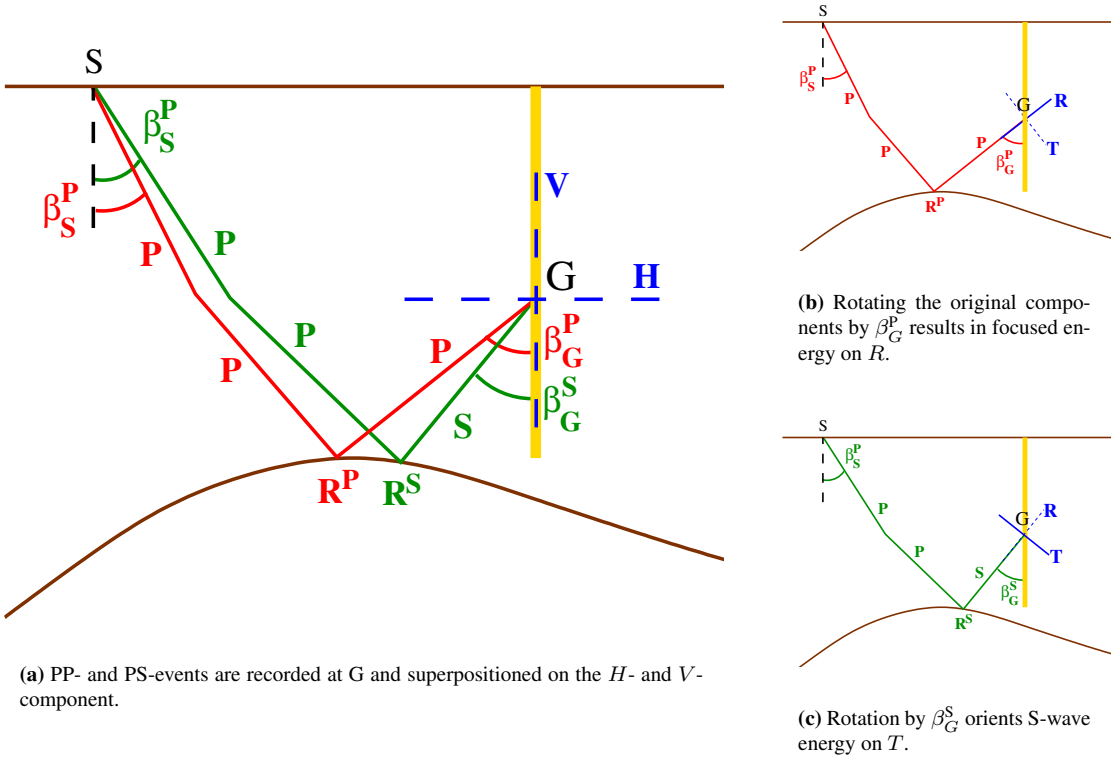

(a) PP- and PS-events are recorded at G and superpositioned on the H- and V-component.

(b) Rotating the original components by β_G^P results in focused energy on R.

(c) Rotation by β_G^S orients S-wave energy on T.

Figure 9: Multicomponent handling

$\beta_G^{P/S}$) also provided by the CRS-stack-based imaging sequence. By these quantities we can approximate the rotation angles $\gamma^{P/S}$ depending on the distance Δz_G off the central ray geophone in the following form:

$$\sin\gamma^{P/S}(\Delta z_G) = \operatorname{sign}(R_{G_{CS}}^{P/S}) \frac{R_{G_{CS}}^{P/S}\sin\beta_G + \Delta z_G}{\sqrt{{R_{G_{CS}}^{P/S}}^2 + 2\,R_{G_{CS}}^{P/S}\,\Delta z_G\,\sin\beta_G + \Delta z_G^2}} \tag{4}$$

with $R_{G_{CS}}^{P/S} = 1/K_{G_{CS}}^{P/S}$. The expression itself is stated in a VSP-adapted way. It can found originally in Höcht et al. (1999).

The potential of this wavefield separation lies not only in the advantage to provide maximum energy for subsequent stacking of CS-,CR-, or CRS-gathers but also in the option to generate two whole new sets of prestack data with separated wavemodes. As a final example I want to show five neighboring multicomponent common shot gathers (see Figures 10(a) to 10(d)) and how they are transformed by the CRS-based separation to contain either radial or transversal energy.

SUMMARY AND OUTLOOK

I presented a recent innovation of CRS-stack-based imaging adapted to the specific needs of a VSP geometry. The method bears the potential of an increased signal-to-noise ratio, data-driven autonomy, but also quality control by the user. The kinematic wavefield attributes calculated from the CRS stacking parameters can serve as constraints for tomography-based approaches to perform building of velocity models but also to limit migration apertures. A comparison between prestack depth migration and postSDM of the CRS results applied on a synthetic but realistic data example reveals that this method is a potent new addition to the box of VSP imaging tools. The option to examine and separate PP- and PS-events should be attractive to a wide audience in research and industry.

Present and future research focuses on the application of the presented workflow with all its presented options to real data and on the comparison to standard processing schemes. A limited aperture Kirchhoff depth migration and *CRS-based redatuming* are two secondary objectives I want to pursue which will further contribute to the variety and utility of the method.

ACKNOWLEDGMENTS

This work was kindly supported by the sponsors of the *Wave Inversion Technology (WIT) Consortium*, Karlsruhe, Germany. I especially wish to thank *Paulsson Geophysical Services Inc. (P/GSI)*, for providing the presented synthetic data and for assisting me in many questions on VSP imaging.

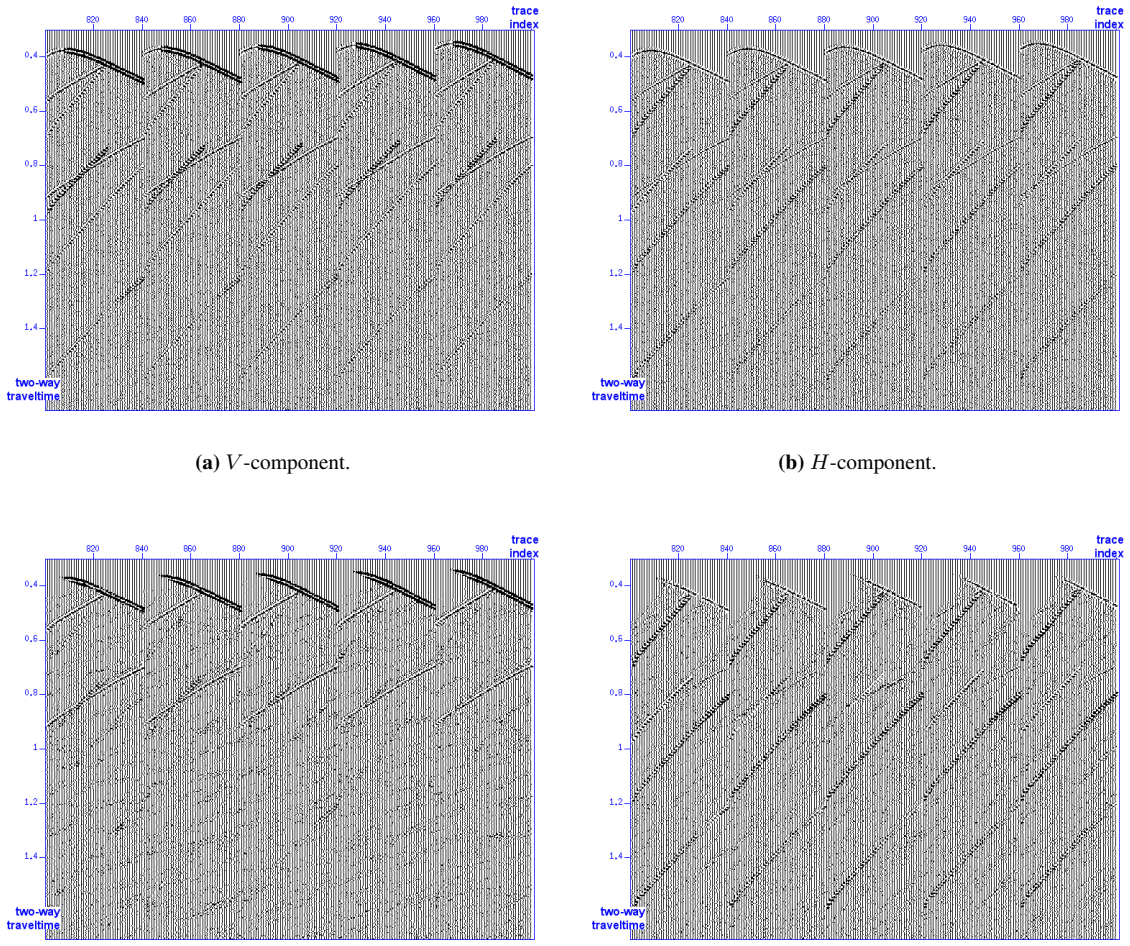

(a) V-component.

(b) H-component.

(c) R-component.

(d) T-component.

Figure 10: Application of the CRS-based wavefield separation on five common shot gathers in the prestack data.

REFERENCES

Boelsen, T. (2005). The Common-Reflection-Surface Stack for arbitrary acquisition geometries and multi-component data – Theory and Application. Master's thesis, Karlsruhe University, http://www.wit-consortium/Downloads.

Červený, V. (2001). *Seismic Ray Theory*. Cambridge Univ. Press, New York, 2001.

Höcht, G., de Bazelaire, E., Majer, P., and Hubral, P. (1999). Seismics and optics: hyperbolae and curvatures. *Journal of Applied Geophysics*, 42(3,4):261–281.

Müller, T. (1998). Common reflection surface (CRS) stack versus NMO/stack and NMO/DMO/stack. In *Extended Abstracts*. 60th Annual Internat. Mtg., Eur. Assn. Geosci. Eng. Session: 1-20.

von Steht, M. (2006). 2D CO CRS imaging for multicomponent data recorded by the VSP geometry. In *Extended Abstracts*. 68th Annual Internat. Mtg., Eur. Assn. Geosci. Eng. Session: P281.

Zhang, Y., Bergler, S., and Hubral, P. (2001). Common reflection surface (CRS) stack for common offset. *Geophysical Prospecting*, 49(6):709–718.